Optical tomography with the equation of radiative transfer

Alexander D. Klose and Andreas H. Hielscher
Departments of Biomedical Engineering and Radiology, Columbia University, New York, New York, USA

Received 10 January 2007
Revised 25 May 2007
Accepted 25 May 2007

Abstract

Purpose – This paper sets out to give an overview about state-of-the-art optical tomographic image reconstruction algorithms that are based on the equation of radiative transfer (ERT).

Design/methodology/approach – An objective function, which describes the discrepancy between measured and numerically predicted light intensity data on the tissue surface, is iteratively minimized to find the unknown spatial distribution of the optical parameters or sources. At each iteration step, the predicted partial current is calculated by a forward model for light propagation based on the ERT. The equation of radiative is solved with either finite difference or finite volume methods.

Findings – Tomographic reconstruction algorithms based on the ERT accurately recover the spatial distribution of optical tissue properties and light sources in biological tissue. These tissues either can have small geometries/large absorption coefficients, or can contain void-like inclusions.

Originality/value – These image reconstruction methods can be employed in small animal imaging for monitoring blood oxygenation, in imaging of tumor growth, in molecular imaging of fluorescent and bioluminescent probes, in imaging of human finger joints for early diagnosis of rheumatoid arthritis, and in functional brain imaging.

Keywords Finite element analysis, Image processing, Radiation, Body systems and organs

Paper type Technical paper

1. Introduction

Over the last decade considerable advances have been made towards tomographic imaging of biological tissue using near-infrared light in the wavelength range of 600-900 nm (Gibson *et al.*, 2005). The light propagation at these wavelengths in biological tissue is governed by the spatial distribution of optical properties such as the scattering, μ_s, and absorption, μ_a, coefficients. The absorption coefficient covers a wide range of values, $\mu_a = 0.01\ldots0.5\,\mathrm{cm}^{-1}$, for near-infrared light mainly depending on the tissue oxygenation level of hemoglobin. The scattering coefficient takes on values in the range of $\mu_a = 20\ldots200\,\mathrm{cm}^{-1}$ (Cheong *et al.*, 1990). Also often use to describe optical properties of tissue is the reduced scattering coefficient, $\mu_s = (1-g)\mu_s$, which is a scaled scattering coefficient that takes into account the mean scattering cosine g (anisotropy factor) of a single scattering event. Typical values of g in tissue are between 0.8 and 0.98 (Cheong *et al.*, 1990).

In optical tomographic imaging, also often referred to as diffuse optical tomography (DOT), one seeks to provide the spatial distribution of these optical properties and

---

This work was supported in part by the National Institute of Arthritis and Musculoskeletal and Skin Diseases (NIAMS – Grant 2R01 AR46255-04), the National Institute of Biomedical Imaging and Bioengineering (NIBIB – Grant 5R01-EB001900), the National Cancer Institute (NCI-grant 5R33-CA91807), and the Ernst-Schering Research Foundation.

International Journal of Numerical Methods for Heat & Fluid Flow
Vol. 18 No. 3/4, 2008
pp. 443-464
© Emerald Group Publishing Limited
0961-5539
DOI 10.1108/09615530810853673

related physiological parameters by probing the tissue with light and measuring the transmitted light distribution on the tissue surface. Over the last decade a variety of different instruments have been developed that perform highly sensitive measurements on various body parts (Schmitz *et al.*, 2002; Lasker *et al.*, 2007; Gulsen *et al.*, 2006; Thompson and Sevick-Muraca, 2003; Schmitz *et al.*, 2000; McBride *et al.*, 2001; Li *et al.*, 2006; Patwardhan *et al.*, 2005; Joseph *et al.*, 2006). In this work, we focus on image reconstruction algorithms that take this data and turn it into two- or three-dimensional spatial maps of optical properties or contrast agent concentration.

State-of-the-art model-based iterative image reconstruction schemes typically consist of two parts:

(1) a forward model for light propagation; and
(2) an inverse model.

The forward model predicts the detector readings on the tissue boundary given a distribution of optical properties inside the medium. The inverse model determines the optical parameters inside the tissue, given a set of detector readings and detector predictions on the boundary of the tissue. The forward and inverse models are iteratively employed within an optimization method. The predicted detector readings of the forward model on the tissue surface are subsequently compared to measured detector readings by defining an objective function, e.g. a χ^2-error norm. The objective function is minimized with an optimization method for non-linear functions, such as conjugate gradient or quasi-Newton methods. The optical parameters at the minimum of the error function are considered as the solution of the inverse problem (Hielscher *et al.*, 1999; Klose and Hielscher, 1999).

In the most general terms, the light propagation in biological tissue can be described by the equation of radiative transfer (ERT) (Duderstadt and Martin, 1979). The ERT is typically solved with some numerical methods since no analytical solutions of the ERT exist for non-uniform media with complex geometries. These numerical methods are either low-order approximations to the ERT, such as the diffusion approximation, or high-order approximations to the ERT, e.g. discrete ordinates (S_N) methods (Carlson and Lathrop, 1968). The spatial discretization of the tissue domain can be performed with either finite-difference (FD), finite-volume (FV), or finite-element (FE) techniques. The diffusion approximation is most widely employed for DOT and has been successfully applied in tissues where $\mu_s \gg \mu_a$ (diffusion regime), e.g. imaging of the female breast or imaging of muscular tissue (Hielscher *et al.*, 1998). However, the diffusion approximation has limited applications when applied to tissue with small geometries, tissue with high absorption, or tissue containing void-like areas. In that case, high-order approximations of the ERT are required such as discrete-ordinates methods.

Several researchers have already worked on solving the forward and inverse problem based on the ERT. For example, the optical parameters of a plane-parallel medium have been estimated from measurements performed on the medium boundary (Elliot *et al.*, 1988; Wang and Ueno, 1989). The interior source distributions of scattering media has been derived in ocean optics or atmospheric problems (McCormick, 1992). A solution method for solving the inverse problem has also been proposed in neutron transport (Larsen, 1981). In biomedical optics, first results of solving inverse problems based on the ERT were shown in the late 1990s. Tomographic imaging of biological tissue with small geometries is encountered, for example, in imaging of human finger joints for early diagnosis of rheumatoid arthritis (RA). It has been shown that reconstructing the spatial map of scattering and absorption coefficients provides valuable clinical information about the condition of finger joints (Scheel *et al.*, 2005). The joint cavity contains a low-scattering fluid that constitutes a non-diffusive regime for near-infrared light. Hence, the small finger geometry and the void-like joint cavity require an ERT-based image reconstruction method (Hielscher *et al.*, 2004). Another application of ERT-based image reconstruction algorithms is imaging of small animals. Small animals are widely used as model for human disease in biomedical research. Optical tomographic methods have shown to be useful in determining various hemodynamic and hemostatic parameters in various disease models (Bluestone *et al.*, 2004a, b; Siegel *et al.*, 2003). Of special interest is currently the use of fluorescence and bioluminescence markers (Klose and Hielscher, 2003; Weissleder and Mahmood, 2001). For example, in fluorescence molecular tomography (FMT) biochemical fluorescent markers are injected into a cancer-bearing mouse, and upon excitation with an external light source the fluorescent marker will emit light. The fluorescent light is detected with a CCD camera on the tissue surface. Subsequently, a spatial map of the fluorescent marker concentration is reconstructed that, e.g. allows to monitor the growth of a tumor or the effectiveness of new anti-cancer drugs. Bioluminescence tomography (BLT) is similar to FMT, however, the molecular probes spontaneously emit light and no excitation with an external light source is necessary. In both cases, ERT-based image reconstruction methods are required due to the small tissue geometries of mice and often high-tissue absorption coefficient at the fluorescence and bioluminescence wavelength.

Light propagation studies in tissue optics based on the ERT have extensively been carried out by researchers (Klose and Hielscher, 1999, 2003, 2002; Hielscher *et al.*, 1998, 2004; Scheel *et al.*, 2005; Aydin *et al.*, 2004, 2005; Khan and Thomas, 2005; Cai *et al.*, 2003; Arridge and Dorn, 2006; Tarvainen *et al.*, 2006, 2005a, b; Dorn, 1998; Ren *et al.*, 2004, 2006; Abdoulaev *et al.*, 2005; Abdoulaev and Hielscher, 2003; Boulanger and Charette, 2005a, b; Klose *et al.*, 2005; Kim and Moscoso, 2006). For example, Hielscher *et al.* and Aydin *et al.* performed numerical studies for assessing the validity of the ERT and the diffusion equation in biological tissue, especially when large absorption coefficients and void-like domains are present (Hielscher *et al.*, 1998; Aydin *et al.*, 2004, 2005; Khan and Thomas, 2005). Hielscher *et al.* (1998) used a diffusion-accelerated FD-S_N method for calculating the light distributions inside a human brain model. Aydin *et al.* (2004, 2005) developed a FE-spherical harmonics (P_N) method for studying light propagation in void-like domains. Khan and Thomas (2005) employed a P_N approximation to the ERT for studying the impact of the refractive index in photon propagation in tissue. The ERT has also been applied to problems in DOT where an inverse scattering or source problems was solved. For example, Klose and Hielscher (2002) used an FD-S_N technique based on the steady-state ERT for reconstructing the scattering and absorption properties in tissue phantoms containing voids. Cai *et al.* (2003) utilized an analytic solution to the steady-state ERT for reconstructing the optical properties in numerical tissue models. Arridge and Dorn (2006) and Tarvainen *et al.* (2006, 2005a, b) developed a hybrid method consisting of a diffusion model and a transport model for optical tomography in order to speed up the image reconstruction process. The ERT has also been applied to DOT in frequency and time domain. Dorn (1998) introduced a generalized algebraic reconstruction technique in conjunction with a FD-S_N method based on the time-dependent ERT for reconstructing the scattering and absorption coefficients in numerical studies. Ren *et al.* (2004, 2006) developed a FV method based on the ERT in frequency domain which reconstructs the absorption and scattering coefficients in numerical tissue models and provides a better means for separating the absorption and scattering coefficients. Abdoulaev *et al.* (2005) presented a constrained optimization technique in the frequency domain for reconstructing optical properties. They also developed a FE even-parity method for DOT (Abdoulaev and Hielscher, 2003). Boulanger and Charette (2005a, b) developed an image reconstruction method based on the time-dependent ERT. Advances have also been made in image reconstruction of fluorescent light source in tissue for optical molecular tomography. Klose *et al.* developed a FD-S_N method and a Delta-Eddington approach for optical molecular tomography that recovers the fluorescent probe concentration distribution (Klose and Hielscher, 2003; Klose *et al.*, 2005). The Delta-Eddington method reduces the number of discrete ordinates of the S_N method leading to a computational speed-up of the image reconstruction. Kim and Moscoso (2006) established an analytical approach for recovering the fluorescent probe distribution in scattering tissue. Most recently, a simplified spherical harmonics (SP-$_N$) method has been proposed by Klose and Larsen (2006) to tissue optics which reduces the number of equations of the P_N technique leading to a transport approximation for highly absorbing media based on coupled diffusion equations.

In the following sections, we will provide an overview of some of the major aspects in implementing ERT-based optical tomography codes, and show some promising applications that illustrate the performance of ERT-based codes.

2. Modeling light transport in biological tissue

The fundamental quantity in tissue optics is the radiance or angular flux of photons, $\Psi(r,\Omega)$, with units of W cm^{-2} sr^{-1}, at the spatial position r and unit direction Ω. The ERT is a balance equation for the angular flux Ψ and is given by the relation:

$$\Omega\cdot\nabla\Psi(r,\Omega)+(\mu_{\mathrm{a}}+\mu_{\mathrm{s}})\Psi(r,\Omega)=\mu_{\mathrm{s}}\int_{4\pi}p(\Omega,\Omega')\Psi(r,\Omega')\mathrm{d}\Omega'. \tag{1}$$

Other quantities besides the radiance Ψ that are included in the ERT are the scattering coefficient, the absorption coefficient, both given in units of cm^{-1}, and the scattering phase function $p(\Omega,\Omega')$ with units of sr^{-1}. The scattering phase function $p(\Omega,\Omega')$ describes the anisotropic scattering behavior of photons in biological tissue and gives the probability that a single photon is deflected by an angle θ. The angle θ encloses the two directions formed by Ω and Ω' in the interval $[0,\ \pi]$ with $\cos\theta=(\Omega\cdot\Omega')$. The expectation value of $\cos\theta$ with $g=\langle\cos\theta\rangle$ is also termed the anisotropy factor g. Furthermore, the phase function p is normalized with:

$$\int_{4\pi}p(\Omega\cdot\Omega')\mathrm{d}\Omega'=2\pi\int_{-1}^{1}p(\cos\theta)\mathrm{d}\cos\theta=1. \tag{2}$$

A commonly applied scattering phase function in tissue optics is the Henyey-Greenstein (HG) phase function p_{HG}, which is given as:

$$p_{\mathrm{HG}}=\frac{1-g^2}{4\pi(1+g^2-2g\cos\theta)^{3/2}}. \tag{3}$$

Biological tissues have an optical refractive index between $n_m = 1.33$ and $n_m = 1.55$ that is different from the refractive index of the surrounding medium, e.g. air ($n_0 = 1$) (Cheong *et al.*, 1990). Therefore, light is partially reflected back into the medium when escaping through the tissue-air interface. The radiance that is reflected back into the medium can be obtained from the following boundary condition:

$$\Psi(r,\Omega) = R(\Omega'\cdot n)\Psi(r,\Omega') + S(r,\Omega) \quad \text{for } \ \Omega\cdot n < 0. \tag{4}$$

The amount of light that is reflected back is determined by the reflectivity R, which is given by Fresnel's law:

$$R = \frac{\sin(\beta-\alpha)}{\sin(\beta+\alpha)} + \frac{\tan(\beta-\alpha)}{\tan(\beta+\alpha)}. \tag{5}$$

The angle α is enclosed by the surface normal vector, $\mathbf{n}$, and the outward direction Ω' of the escaping radiance, whereas the angle β is enclosed by the normal vector and the outward direction Ω'' of the refracted light. The direction Ω'' of the refracted light is determined by means of Snell's law for any given outward direction Ω'. In addition, exterior light sources $S(r,\Omega)$, such as laser diodes for probing the tissue, constitute additional boundary sources besides the partially reflected light. More details about the ERT-based light propagation model can be found in Klose *et al.* (2005).

The integral of the radiance $\Psi(r,\Omega)$ over all directions Ω at a single point r inside tissue yields the fluence Φ with units of W cm^{-2}:

$$\Phi = \int_{4\pi} \Psi(r,\Omega)\mathrm{d}\Omega. \tag{6}$$

The physical quantity that is measured by a detector at the tissue surface is the partial photon current, J^+, in units of W cm^{-2}, which is given by:

$$J^+ = \int_{\Omega\cdot n>0} [1 - R(\Omega\cdot n)](\Omega\cdot n)\Psi(r,\Omega)\mathrm{d}\Omega. \tag{7}$$

The measured partial current becomes input to an image reconstruction technique which subsequently reconstructs the optical parameters, such as the absorption and scattering coefficients.

The ERT, as shown by equation (1), is used for transillumination imaging in DOT, where laser sources are placed on the tissue boundary and no interior light sources are present. In the case of fluorescence tomography, FMT, of light emitting fluorophores, a second ERT is needed that describes the propagation of fluorescent light after fluorophores have been excited with an external light source at excitation wavelength λ^x. Therefore, we obtain the following ERT at the emission wavelength λ^m:

$$\Omega\cdot\nabla\Psi(r,\Omega) + (\mu_\mathrm{a} + \mu_\mathrm{s})\Psi(r,\Omega) = \frac{1}{4\pi}\mu_\mathrm{a}^{x\rightarrow m}\eta\Phi^x + \mu_\mathrm{s}\int_{4\pi} p(\Omega,\Omega')\Psi(r,\Omega')\mathrm{d}\Omega'. \tag{8}$$

The excitation field Φ^x is calculated with equations (1) and (6). The energy of the excitation field at λ^x is partially absorbed by the fluorophore having an absorption coefficient $\mu_\mathrm{a}^{x\rightarrow m}$. The fluorophore absorption coefficient is determined by the fluorophore concentration, c, inside tissue and the extinction coefficient, ε, at the excitation wavelength λ^x. The term η represents the quantum yield of the fluorophore, which determines the amount of light that will be re-emitted at λ^m for a given amount of excitation light. The partial current, J^+, of the fluorescence light will be detected at the tissue boundary for different positions of excitation sources. An image reconstruction algorithm tries to recover the spatial position and concentration of the unknown fluorophore distribution.

A third application of the ERT in tissue optics is BLT for molecular imaging of bioluminescent reporter probes in small animal tissue. BLT is similar to FMT, except that no externally imposed excitation field Φ^x is given. Bioluminescent sources utilize biochemical energy for the optical excitation of probes. The ERT for bioluminescent light originating from light emitting sources $Q(r)$ inside tissue is given by:

$$\Omega \cdot \nabla\Psi(r,\Omega) + (\mu_a + \mu_s)\Psi(r,\Omega) = Q(r) + \mu_s \int_{4\pi} p(\Omega,\Omega')\Psi(r,\Omega')d\Omega'. \tag{9}$$

The boundary condition contains only light sources due to the partial light reflection at the tissue-air interface:

$$\Psi(r,\Omega) = R(\Omega' \cdot n)\Psi(r,\Omega') \quad \text{for} \ \ \Omega \cdot n < 0. \tag{10}$$

The partial current, J^+, of bioluminescent light is measured at the tissue boundary.

3. Numerical methods

3.1 Finite-difference discrete-ordinates method

The ERT, equation (1), can be solved with a FD-S_N method that converts the integro-differential equation into a system of algebraic equations. The direction Ω is replaced with a set of discrete ordinates Ω_k with full level symmetry. The total number, K, of ordinates Ω_k is given by $K = N(N + 2)$ and N being the number of direction cosines of the S_N method. The integral in the ERT is approximated with a quadrature rule:

$$\int_{4\pi} p(\Omega \cdot \Omega')\Psi(\Omega', r)d\Omega' \cong \sum_{k'=1}^{K} w_{k'} p_{kk'} \Psi_{k'}(r), \tag{11}$$

where w_k are weights determined by full level symmetry of the ordinates. The angular discretization yields a set of K coupled differential equations for the radiance $\Psi_k(r)$ in the directions Ω_k:

$$\Omega_k \cdot \nabla\Psi_k(r) + (\mu_a + \mu_s)\Psi_k(r) = \mu_s \sum_{k'=1}^{K} w_k p_{kk'} \Psi_{k'}(r) \tag{12}$$

The continuous spatial variable r is discretized on a three-dimensional Cartesian grid with grid points at $r = (x_m, \ y_n, \ z_l)$ and (m, n, l) being grid point indices of $[(1\ldots M), (1\ldots N), (1\ldots L)]$. The grid spacing between adjacent grid points is given by Δx, Δy, and Δz. The spatial derivatives in equation (12) are substituted with first-order FD approximations, known as step method, or with second-order approximations, given by the diamond method. The resulting algebraic system of equations is solved by employing a source iteration (SI) method.

3.1.1 Delta-Eddington method. In general, the HG phase function can be expanded into a series of Legendre polynomials $P_n(\cos\theta)$:

$$p_{\mathrm{HG}}(\cos\theta) = \frac{1}{4\pi}\sum_{n=0}^{N}(2n+1)b_n P_n(\cos\theta) \tag{13}$$

with coefficients:

$$b_n = 2\pi\int_{-1}^{1} p_{\mathrm{HG}}(\cos\theta)P_n(\cos\theta)\mathrm{d}\cos\theta = g^n. \tag{14}$$

An isotropic-scattering medium is described by $b_0 = 1$ and $b_n = 0$. The anisotropy factor g in equation (14) equals the coefficient $b_1 = g$ for anisotropically scattering media. However, for highly anisotropically scattering media ($g > 0.8$), such as biological tissue, the computational burden becomes very large for $\mathrm{S_N}$ and $\mathrm{P_N}$ methods. Many Legendre polynomials $\mathrm{P_N}$ and discrete ordinates Ω_k are needed to account for a sufficiently accurate angular discretization of the radiance. If the number K of used discrete ordinates is too small, the condition (2) for a normalized phase function is not satisfied anymore:

$$\sum_{k'=1}^{K} w_k p_{kk'} p(\Omega_k \cdot \Omega_{k'}) \neq 1. \tag{15}$$

Consequently, the use of small numbers of discrete ordinates or Legendre polynomials leads to false scattering and affects the accuracy of $\mathrm{S_N}$ and $\mathrm{P_N}$ techniques.

Therefore, a Delta-Eddington method can be employed that reduces the number of discrete ordinates and Legendre polynomials by transforming the phase function into two separate terms (Joseph *et al.*, 1976):

1. a fraction f of scattered photons within a collimated laser beam is described by a δ-function; and
2. the remaining fraction $(1 - f)$ out of the collimated laser beam scattered photons is described by a new HG phase function p'_{HG}:

$$p_{\mathrm{HG}}(\cos\theta) \cong p_{\delta-\mathrm{HG}}(\cos\theta) = (1-f)p'_{\mathrm{HG}}(\cos\theta) + \frac{1}{2\pi}f\delta(1-\cos\theta) \tag{16}$$

The new HG phase function p_{HG} can also be expanded into a series of Legendre polynomials:

$$p'_{\mathrm{HG'}}(\cos\theta) = \frac{1}{4\pi}\sum_{n=0}^{N}(2n+1)b'_{n'}P_n(\cos\theta). \tag{17}$$

Substitution of the HG phase function (17) into equation (16) and replacing the δ-function with a series of Legendre polynomials gives the new coefficients:

$$b'_n = \frac{b_n - f}{1 - f} \tag{18}$$

with $f = g^{N+1}$. N denotes the number of terms after the series expansion in equation (17) is terminated. The ERT is now re-written by inserting equation (16) into equation (1):

$$\Omega \cdot \nabla \Psi(r, \Omega) + (\mu_a + (1 - f)\mu_s)\Psi(r, \Omega) = (1 - f)\mu_s \int_{4\pi} p'_{HG}(\Omega, \Omega')\Psi(r, \Omega')d\Omega'. \quad (19)$$

Equation (19) can be applied to highly anisotropically scattering biological tissue but by avoiding the use of S_N methods with large N. More details can be found in Klose *et al.* (2005).

3.2 Finite volume discrete-ordinates method

Complicated tissue geometries can easily be handled by arbitrary triangulations within a FV framework (Ren *et al.*, 2004). Furthermore, FV methods ensure the conservation of radiation energy in a discrete sense, which is important to transport calculations. A cell-centered version of a FV method has recently been implemented for DOT in frequency domain (Ren *et al.*, 2006). The ERT in frequency domain is given by:

$$\Omega \cdot \nabla \Psi(r, \Omega) + \left(\mu_a + \mu_s + \frac{i\omega}{c}\right)\Psi(r, \Omega) = \mu_s \int_{4\pi} p(\Omega, \Omega')\Psi(r, \Omega')d\Omega' \quad (20)$$

with c being the speed of light and ω being the frequency of an amplitude-modulated light source. A mesh consisting of polyhedral elements covers the entire computational spatial domain. The radiance Ψ takes an average value Ψ^C inside a control cell C, which is an element with volume V_C of the mesh:

$$\Psi^C = \frac{1}{V_C} \int_{V_C} \Psi(r, \Omega)dV. \quad (21)$$

Integrating equation (20) for each discrete ordinate Ω_k over cell C and using the divergence theorem on the first term yields:

$$\sum_i F_{ki}^C + \left(\mu_a + \mu_s + \frac{i\omega}{c}\right) V_C \Psi_k^C = V_C \mu_s \sum_{k'=1}^{K} w_k p_{kk'} \Psi_{k'}^C(r) \quad (22)$$

with:

$$F^C = \int_{\partial C} \Omega_k \cdot n_C \Psi_k \, dC$$

and i being the index of all neighboring cells C_i. Equation (22) can be cast into a complex-valued matrix equation for all control cells C:

$$\mathbf{A}\Psi = \mathbf{S}\Psi + \mathbf{B}. \quad (23)$$

The matrix (**A**-**S**) is neither symmetric nor positive definite. Therefore, a GMRES method is employed for solving the system of algebraic equations in equation (23). Finally, it should be noted that the FV discretization reduces to an upwind FD scheme on usual FD grids. More details concerning the FV approach can be found in Ren *et al.* (2004, 2006).

3.3 Finite-element even-parity method

Besides, FD and FV methods, FE methods can be employed. We will demonstrate the derivation of the even-parity equations for the general case of interior sources. The special case $Q = 0$ pertains to transillumination tomography with boundary sources S. The ERT (1) as part of an even-parity approach with interior sources Q can be written for all ordinates $-\Omega$ as follows (Abdoulaev and Hielscher, 2003):

$$-\Omega\cdot\nabla\Psi(r,-\Omega)+(\mu_{\mathrm{a}}+\mu_{\mathrm{s}})\Psi(r,-\Omega)=Q+\mu_{\mathrm{s}}\int_{4\pi}p(-\Omega,\Omega')\Psi(r,\Omega')d\Omega'. \quad (24)$$

Adding and subtracting equations (24) and (1) with interior sources yields a system of two-coupled equations:

$$\begin{aligned}\Omega\cdot\nabla\Psi^{-}(r,\Omega)+(\mu_{\mathrm{a}}+\mu_{\mathrm{s}})\Psi^{+}(r,\Omega)&=Q+\mu_{\mathrm{s}}\int_{4\pi}p^{+}(\Omega,\Omega')\Psi^{+}(r,\Omega')\mathrm{d}\Omega' \quad (25)\\ \Omega\cdot\nabla\Psi^{+}(r,\Omega)+(\mu_{\mathrm{a}}+\mu_{\mathrm{s}})\Psi^{-}(r,\Omega)&=Q+\mu_{\mathrm{s}}\int_{4\pi}p^{-}(\Omega,\Omega')\Psi^{-}(r,\Omega')\mathrm{d}\Omega',\end{aligned}$$

where the superscripts " $-$ " and " $+$ " denote even and odd components of a function (Ψ and p) with respect to the ordinates Ω:

$$F^{\pm}(r,\Omega)=\frac{F(r,\Omega)\pm F(r,-\Omega)}{2}. \quad (26)$$

One can rewrite equation (25) in the following operator form:

$$\Omega\cdot\nabla\Psi^{\mp}(r,\Omega)+H_{\pm}\Psi^{\pm}(r,\Omega)=Q \quad (27)$$

where the operators are defined as:

$$H_{\pm}f(r,\Omega)=(\mu+\mu_{\mathrm{s}})f(r,\Omega)-\mu_{\mathrm{s}}\int_{4\pi}p^{\pm}(\Omega\cdot\Omega')f(r,\Omega')\mathrm{d}\Omega'. \quad (28)$$

After exclusion of Ψ^{-} from equation (28) one arrives at:

$$\begin{aligned}&-\Omega\cdot\nabla\Big\{H_{-}^{-1}\big[\Omega\cdot\nabla\Psi^{+}(r,\Omega)\big]\Big\}+H_{\pm}\Psi^{\pm}(r,\Omega)\\ &=Q^{+}(r,\Omega)-\Omega\cdot\nabla\Big\{H_{-}^{-1}Q^{-}(r,\Omega)\Big\}.\end{aligned} \quad (29)$$

Equation (29) is solved by inverting the operator H_{-} explicitly. In case of isotropic scattering H_{-} can easily be inverted since we have the simplified relation $H_{-}^{-1}f=\left(\mu_{\mathrm{a}}+\mu_{\mathrm{s}}\right)^{-1}f$. If the source Q is also isotropic then we arrive at:

$$-\Omega\cdot\nabla\left([\mu_{\mathrm{a}}+\mu_{\mathrm{s}}]^{-1}\Omega\cdot\nabla\Psi^{+}\right)+(\mu_{\mathrm{a}}+\mu_{\mathrm{s}})\Psi^{+}(r,\Omega)=Q(r)+\frac{\mu_{\mathrm{s}}}{4\pi}\int_{4\pi}\Psi^{+}(r,\Omega')\mathrm{d}\Omega'. \quad (30)$$

The integral in equation (30) can be approximated by a discrete ordinates quadrature formula. The resulting set of algebraic equations is then solved with a Galerkin FE method.

4. Image reconstruction

4.1 Unconstrained nonlinear optimization

In general, the spatial distributions of optical parameters, μ_{a} and μ_{s}, in DOT and the fluorophore concentration, *c*, in FMT can be reconstructed with nonlinear optimization techniques that minimize an objective function φ. The objective function describes the difference between the measured data, Y_{d}, and predicted partial current, J_d^+, for all N source-detector pairs:

$$\varphi(\mu) = \frac{1}{N}\sum_{d}^{N} \frac{\left(Y_d - J_d^+(\mu)\right)^2}{\sigma_d^2}. \tag{31}$$

The predicted data J_d^+ are calculated by equation (1) or equation (8), respectively. Gradient-based optimization techniques have been proven to be computationally efficient for large-scale optimization problems. Typically, an optimization problem of 10^3-10^5 unknown optical parameters needs to be solved in DOT. Gradient-based optimization techniques use the gradient $\nabla\phi$ of the objective function for calculating a search direction u_k and a step length α_k to find a new update of optical parameters μ_{k+1}. An updating scheme determines, for example, a new estimate of the sequence of optical parameters:

$$\mu_{k+1} = \mu_k + \alpha_k u_k. \tag{32}$$

Therefore, calculating the new estimate is broken up into two tasks:

(1) finding a proper step length α_k; and
(2) calculating the search direction u_k.

Furthermore, gradient-based optimization algorithms share the following general form:

(1) Start with an initial guess μ_O of the solution.
(2) If the objective function $\phi(\mu_k)$ is minimal, then stop.
(3) Determine an improved estimate $\mu_{k+1} = \mu_k + \alpha_k u_k$.
(4) Go to (2).

Once the minimum is found, the final result μ_{k+1} is the distribution of the optical parameters.

4.1.1 Adjoint differentiation. The optimization method requires calculating the derivative $\nabla\phi$ of the objective function that is a function of 10^3-10^5 variables. Using numerical difference schemes for the derivative computation have proven to be too time-consuming. Therefore, an adjoint differentiation technique, also termed as computational or algorithmic differentiation in the reverse direction, can be employed that is directly applied to the existing numerical code of the forward model in order to ease the computational burden. The main advantage of this approach is that the gradient can be calculated according to simple rules at a level of single steps in the forward code instead of solving an adjoint ERT that constitutes an entire new numerical problem. The forward model of light propagation based on the SI method, that provides a solution to the ERT and a value of the objective function for a given optical parameter distribution, is decomposed into a sequence of single differentiable functions. This sequence of functions is built up in the forward direction as the solution of the forward model is computed. Thus, the objective function is a composition of Z functions of all SI steps:

$$\varphi = (\Psi^Z \circ \Psi^{Z-1} \circ \cdots \circ \Psi^{z+1} \circ \Psi^z \circ \cdots \circ \Psi^0). \tag{33}$$

The operation "∘" is defined as a composite function:

$$\Psi^{z+1} \circ \Psi^z(\mu) = \Psi^{z+1}(\Psi^z(\mu), \mu). \tag{34}$$

Starting with an initial input vector μ a value of the objective function can be obtained according to equation (33). That also defines the forward direction of the forward algorithm. Applying systematically the chain rule of differentiation to each single function of equation (33) in the reverse direction a numerical value of the derivative of the objective function with respect to the optical parameters is obtained:

$$\frac{\partial(\Psi^Z \circ \Psi^{Z-1} \circ \cdots \circ \Psi^z)}{\partial \mu} = \frac{\partial \Psi^z}{\partial \mu} \frac{\partial \Psi^{z+1}}{\partial \Psi^z} \cdots \frac{\partial \Psi^{Z-1}}{\partial \Psi^{Z-2}} \frac{\partial \Psi^{Z-1}}{\partial \Psi^Z} \tag{35}$$

The final result of equation (35) supplies the search direction u_k of equation (30). More details can be found in Klose *et al.* (2005):

4.2 Constrained optimization

Most recently, Abdoulaev *et al.* (2005) have introduced a constrained optimization technique to DOT based on the ERT. Instead of solving the optimization problem in an iterative manner, where the ERT is repeatedly solved for updates μ_{k+1}, the constrained optimization method solves the ERT and the optimization problem simultaneously. This kind of constrained optimization technique promises a much faster solution in DOT.

A Lagrangian functional L is introduced with the relation:

$$L(\mu, \Psi, \lambda) = \varphi(\mu, \Psi) - \langle \lambda, G(\mu, \Psi) \rangle \tag{36}$$

where λ is the Lagrange multiplier. $G(\mu, \Psi)$ is an operator that represents the light propagation model based on the ERT including its boundary condition. The quantities μ and Ψ denote all admissible optical properties and solutions of the forward problem. Furthermore, a solution to the optimization problem of φ satisfies the following optimality conditions for L:

$$\frac{\partial L}{\partial \mu}(\mu, \Psi, \lambda) = 0, \quad \frac{\partial L}{\partial \Psi}(\mu, \Psi, \lambda) = 0, \quad \text{and} \quad G(\mu, \Psi) = 0. \tag{37}$$

This approach has already been proven to be very successful in other applications such as shape design in aerodynamic and optimal control of incompressible flows (Biegler *et al.*, 2003), however, has not been widely applied and tested in optical tomography.

4.3 Ill-posedness and regularization

Small changes or variations in the measurement data or an incorrect forward model cause a relatively large change in the image reconstruction result. Therefore, the objective function (31) will be extended by an additional regularization term P with regularization parameter or hyper-parameter γ:

$$\varphi(\mu) = \frac{1}{N}\sum_{d}^{N} \frac{\left(Y_d - J_d^{+}(\mu)\right)^2}{\sigma_d^2} + \gamma P(\mu) \tag{38}$$

The function P represents a priori information about the solution μ. For example, additional anatomical information could be included into the image reconstruction process. Furthermore, constraints on the optical parameters could be used in order to limit the unknown search space (Hielscher and Bartel, 2001). Most recently, Gu *et al.* (2007) have discussed the detection limits of tissue inhomogeneities with varying optical parameters, sizes, and locations. Similar studies on the quantification and localization accuracy have also been performed for a light propagation model based on the diffusion approximation to the ERT and a Monte-Carlo model (Boas *et al.*, 1997; Toronov *et al.*, 2003). These studies provide an insight into the potentials and limitations of DOT and the ill-posed nature of its image reconstruction algorithms.

5. Examples in biomedical research

5.1 Imaging of voids in finger joints for diagnosis of early rheumatoid arthritis

RA is one of the most common diseases of human joints of the hands and feet. RA is a progressive disease and is characterized by an inflammation process that originates in the inner membrane (synovial membrane or synovium) of the joint capsule and spreads to other parts of the joint. Routine imaging techniques for early diagnosis do not exist. However, first clinical results of optical techniques show that DOT might facilitate the diagnosis of early stages of RA (Scheel *et al.*, 2005; Hielscher *et al.*, 2004). Information about the optical properties of the synovium, obtained from DOT, could be used to distinguish between healthy and early rheumatoid conditions. Since, we have void like areas (synovial fluid) inside the finger joint, ERT-based reconstruction methods are advantageous.

For measurements the hand of a patient was placed in a specifically designed imaging chamber. A laser diode illuminated the interior side of a single finger joint at 11 different positions with wavelength at 675 nm. A detector measured the transmitted partial current on the posterior side of the joint at 16 different positions. An image reconstruction method based on a FD-S_8 method reconstructed the optical properties within a sagittal slice of the finger joint. The FD grid covered a cross-sectional area of 4×2.1 cm of the finger with 81×43 grid points. The detectors were placed on the bottom of the grid along the boundary.

Figure 1(a) shows a sagittal magnetic resonance image (MRI) of a human finger joint with joint cavity in the center of the image. The top of the image depicts the interior side where laser sources were placed and the bottom of the images constitutes the posterior side of the finger with the detector scan. The finger tip is towards the right of the image. Figure 1(b) and (c) show the reconstructed sagittal images of the scattering coefficient of two different finger joints. Figure 1(b) shows a healthy finger joint with small scattering coefficients in the center of the image. Figure 1(c) shows a finger joint affected by RA. The scattering coefficient is elevated in the center of the image due to an inflammation of the joint capsule. More details about first clinical studies are given by Scheel *et al.* (2005) and Hielscher *et al.* (2004).

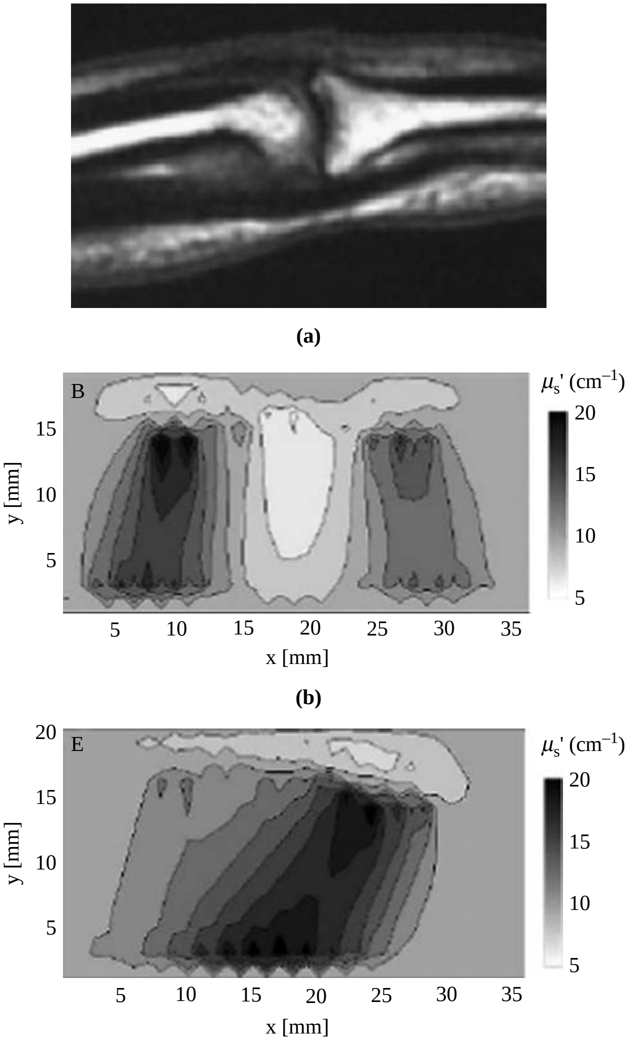

(a)

(b)

(c)

Notes: The finger tip is towards the right. The cavity between the two bones is filled with clear synovial fluid. Sagittal images of the reconstructed scattering coefficient of human fingers in b) healthy stage and c) rheumatoid stage. Small μ_s of the synovial fluid are visible in the center of the image in b). Adjacent isolines are separated by μ_s =2 cm^{-1}. This diagram is reproduced from the only available original

Figure 1.
MRI of a human finger joint with interior side on top

5.2 Imaging of tumor hemodynamics

Over the past decade considerable effort has been put into the development of small animal imaging systems. This work has been motivated by advances in animal models of human diseases and the progress in their transgenic manipulation

(Pomper, 2002; Hielscher, 2005). The goal of many of these novel imaging systems is to noninvasively monitor the temporal as well as spatial progression of disease and other biological processes. Optical imaging techniques have shown great promise in this regard. Though offering poorer spatial resolution than, for example, micro-CT or MRI, optical methods can be used to measure physiologically important chromophore concentrations such as oxyhemoglobin (HbO_2) and deoxyhemoglobin (Hb) with high-temporal resolution (Bluestone *et al.*, 2004a, b; Culver *et al.*, 2003). Furthermore, optical methods are also sensitive to blood volume changes, scattering properties, and can be used in combination with molecular markers (Graves *et al.*, 2004). Temporal resolution in the range of 1-50 Hz can be achieved relatively easily, allowing for relatively fast completion of complex imaging protocols.

One promising application is the monitoring of hemodynamic effects during cancer treatment in mouse models. The following examples describe a study in which we imaged the early onset of drug-tissue interaction. To study these effects, we orthotopically implanted kidney tumor cells in 10 NCR athymic nude mice. Tumors were allowed to grow for 52 days, during which the growth was monitored with MRI (Figure 2(a)) once a week and with optical tomography, twice a week. On the 52nd day a treatment schedule consisting of 0.1 cc anti-VEGF injections twice a week was begun. Optical tomographic data sets were obtained every 0.4 s from 5 min before until 50 min after drug injection. Before the imaging session the animal was anesthetized with ketamine and one end of a thin cannula (PE-10) was inserted into the intraperitoneal cavity. The other end was attached to a needle on a 0.5 cc syringe filled with the VEGF antagonist. In this way the treatment could be administered during the optical scan without removing the animal

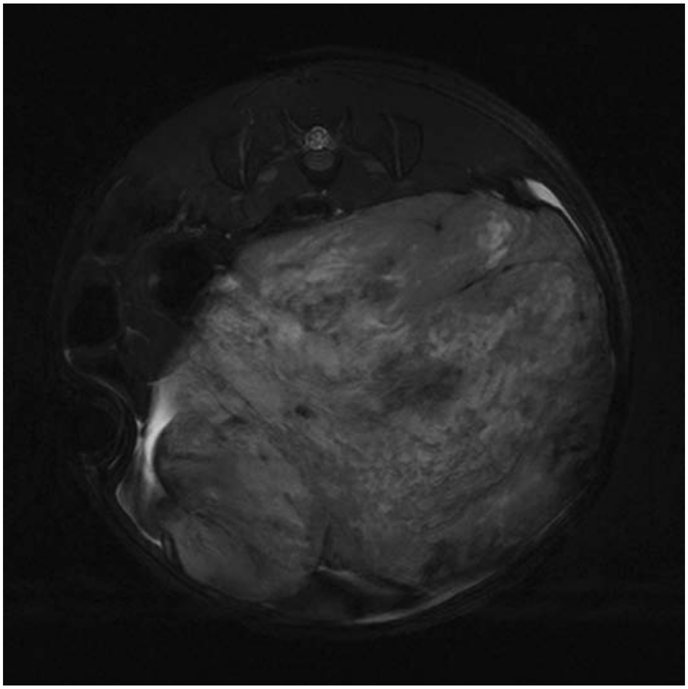

Figure 2.
T2 weighted MR image showing large tumor (the bright mass) of mouse that was given the treatment scan

from the optical imaging probe. In addition to these dynamic studies, optical tomographic images were obtained 24 and 96 h after the injection.

For the optical tomographic measurements we employed a continuous wave mode, dynamic near-infrared optical tomographic (DYNOT) instrument (Schmitz *et al.*, 2002). Laser light at two wavelengths (wavelengths $\lambda_1 = 760$ and $\lambda_2 = 830$ nm) were delivered to 24 source fiber bundles via an optical (de-)multiplexing switch, which allows light to be sequential delivered to different positions. The fibers of the instrument were coupled to an optical imaging probe consisting of a hollow Delrin cylinder (diameter = 5 cm, height = 10 cm) and two fiber-holding rings, which allow the ends of the fibers to be in contact with the surface of the cylinder and can be slid up and down the cylinder to adjust the vertical position of the fibers. Each of the two rings had 24 holes drilled, spaced 15° apart allowing 12 source and 12 detector fibers arranged in an alternating pattern for a total of 24 sources, 24 detectors and thus 576 source detector pairs (Figure 2(b)). About 2.5 full tomographic data sets per seconds, involving all 576 source-detector pair readings of light intensity, were acquired.

The cylinder was partially filled with 1 percent Intralipid which was used as a matching fluid in order to reduced edge effects during image reconstruction. The 1 percent Intralipid was obtained by diluting 10 percent Intralipid (Sigma-Aldrich Corp. St Louis, MO). The mouse was fixed in an anaesthesia nose cone which was suspended from a stereotaxic frame and allowed the mouse to be lowered into the cylinder. Before placement in the optical probe the syringe was stabilized on a surface so that the treatment injection could be administered through the cannula with causing minimal movement inside the probe. The rings, separated by 1.3 cm, were adjusted so that the tumor was in between the two rings. After the mouse was placed in the probe, the optimal detector gain settings were found for each source detector pair. Subsequently, the optical scan was performed continuously for approximately 50 min.

From the 55-minute time-series data, blocks of 400 points (160 s) were taken and averaged at the beginning of the experiment and then every 4 min starting immediately after injection. This data was input into our model-based iterative reconstruction algorithm based on a FD-S_N implementation of the time-independent ERT. Examples of reconstructed absorption images at $\lambda = 760$ nm are shown in Figure 3. The large circular shape corresponds to the cylinder cross-section. Small areas of high absorption on the edge of the circle are source boundary artifacts. The mouse was located with back against the rear of the cylinder (top of image). Figure 3(a)-(e) shows the absorption coefficient image for the mouse at various time points from just prior to injection to 32 min after injection. The area of high absorption is collocated with the tumor as confirmed with MRI. Figure 3(f)-(j) shows images, which represent the original absorption image 3(a) minus the absorption images at each of the various time points. At 8 min after drug injection (Figure 3(c) and (h)) one can observe a decrease in absorption around the periphery of the tumor and an increase in absorption inside the tumor. A decrease in the absorption coefficient inside the tumor occurs there after. By 32 min after injection a large decrease in absorption coefficient is observed inside the tumor. In most cases, we observed that this or an even stronger decrease is still present 24 h after treatment.

Using this data together with measurements obtained at 830 nm it is possible to derive values for physiologically important parameters such as changes in oxy-, deoxy-, and total-hemoglobin concentration. Figure 4 shows these values for the

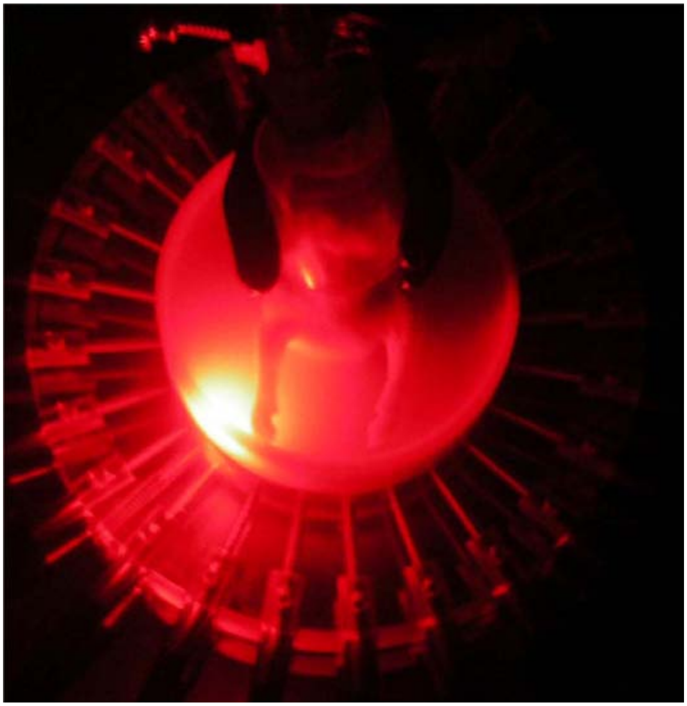

Figure 3.
Photograph of a mouse in the experimental set-up consisting of 24 sources and 24 detectors

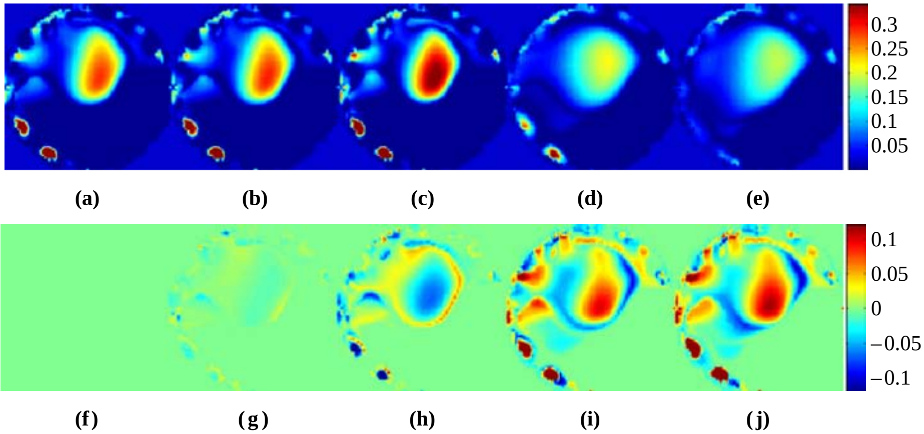

Figure 4.
Maps of the absorption coefficient

Notes: (μ_α in units of cm^{-1}) at λ =760 nm for a) 0, b) 4, c) 8, d) 16, and e) 32 minutes after injection; and changes in absorption coefficient ($\Delta\mu_\alpha$ in units of cm^{-1}), with respect to Figure 4 a), for f) 0, g) 4, h) 8, i) 16, and j) 32 minutes after injection

8-minute time point. Here we can see that in the center of the tumor HbO_2 is reduced while Hb concentration is increased. Total hemoglobin concentrations (HbT) are increased on the periphery of the tumor and slightly decreased in the center (Figure 5).

In other studies, we looked at long-term effects of the drugs and confirmed that a reduction in blood volume is not a short-term effect but is still visible days after the treatment (Masciotti *et al.*, 2005; Glade-Bender *et al.*, 2003). This finding was in agreement with other studies that have shown disrupting VEGF signaling, which is responsible for angiogenesis, and can attenuate or even abolish tumor vasculature, producing marked tumor regression (Frischer *et al.*, 2004).

5.3 Imaging of fluorescent sources in small animals

Optical molecular imaging uses near-infrared fluorescent probes for studying molecular processes in living organisms (Weissleder and Mahmood, 2001). A fluorescent biochemical marker is injected into a small animal, such as a nude mouse, and will emit near-infrared light upon excitation by an external light source. From measurements of the partial current at the tissue surface one seeks to determine the spatial concentration distribution of the marker inside the tissue.

An ERT-based image reconstruction method is well-suited for small animal imaging since it is an accurate light propagation model for small tissue geometries and small source-detector separations. Therefore, we have developed a tomographic reconstruction method for fluorescent light sources based on our FD-S_N Delta-Eddington light propagation model. We have tested the performance of the image reconstruction method with an *in vivo* mouse model for Lewis Lung Carcinoma (LLC) (Klose *et al.*, 2004). The animal was injected with a Cy5.5-based fluorescent probe (Cy5.5: quantum yield $\eta = 0.28$, extinction $\varepsilon = 250{,}000\,\mathrm{M\,cm}^{-1}$) with high sensitivity to cathepsins. Cathepsins are lysosomal enzymes for protein degradation, which can also be present in the extracellular space of cancerous cells. Fluorescent molecular probes are exposed to these cathepsins inside the extracellular matrix and are subsequently activated and emit fluorescent light. For the data acquisition the mouse was immersed into an imaging chamber containing a scattering matching fluid. The imaging chamber had a size of $4 \times 4 \times 1.3\,\mathrm{cm}^3$. One side of the chamber was illuminated with light at wavelength 674 nm emerging from 46 fibers arranged in a symmetric pattern (crosses in Figure 6). A CCD camera captured the excitation and fluorescence light at wavelength at 694 nm on the side opposite to the illuminating fibers (circles in Figure 6). Figure 6 shows a surface-weighted fluorescence image of the mouse model with a LLC on the left side, but no spatial information of the fluorophore concentration is available. Figure 6 show tomographic images of the fluorophore concentration at different depths.

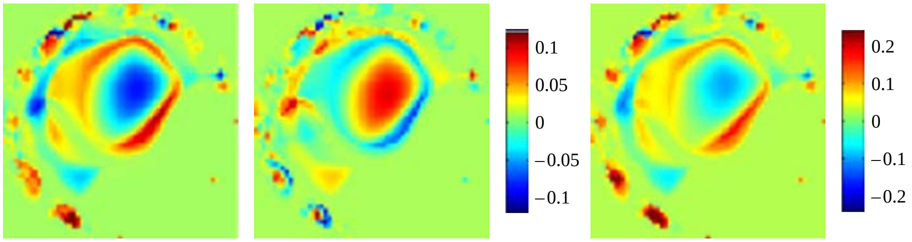

Figure 5.
Changes (in units of mM) in HbO_s (left), Hb (middle), and HbT (right) as calculated with data obtained at 760 and 830 nm

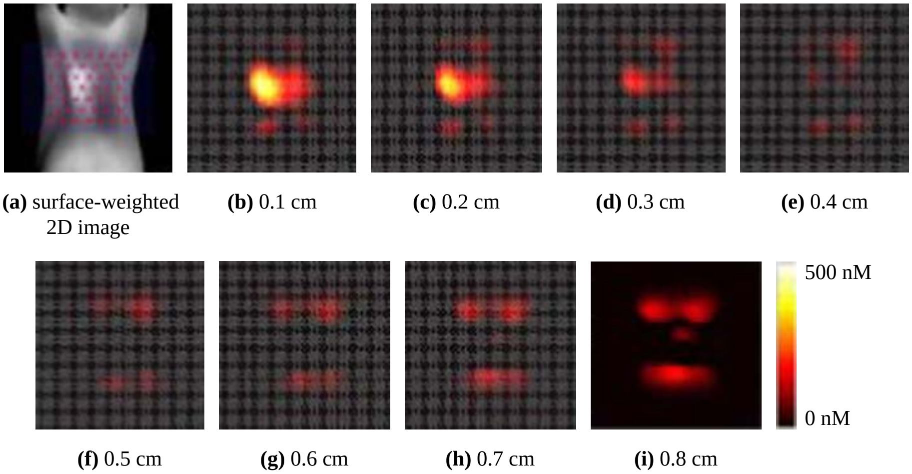

(a) surface-weighted 2D image **(b)** 0.1 cm **(c)** 0.2 cm **(d)** 0.3 cm **(e)** 0.4 cm

(f) 0.5 cm **(g)** 0.6 cm **(h)** 0.7 cm **(i)** 0.8 cm

Notes: *c* [nM] are shown in b)-i), whereas a) shows the surface-weighted fluorescence. The reconstructed parallelepiped with immersed mouse has a size of $4 \times 4 \times 1.3$ cm^3. Top slice in b) is closest to the detector plane ($z = 0.1$ cm). Last slice in i) is deepest inside the tissue ($z = 0.8$ cm) and closest to the source plane ($z = 1.3$ cm). The lung carcinoma can be seen in the three top slices b)-d). This diagram is reproduced from the only available original

Figure 6.
Eight slices of reconstructed fluorophore concentration

6. Summary

We have presented various approaches to the image reconstruction problem encountered in optical tomography of highly scattering biological tissue. We specifically focused on algorithms that employ the ERT to model light propagation in this medium. By not relying on the diffusion approximation, these algorithms have the potential to provide more accurate solutions in cases where the diffusion approximation fails, such as in media with small geometries or media containing void-like areas. We presented implementation of such algorithms with FD, FV, and FE schemes, and discussed constrained as well as unconstrained optimization schemes. To illustrate the performance of these codes we showed some *in vivo* applications from studies concerning the detection of RA in human finger joints, monitoring hemodynamic responses in tumor vasculature in response to anti-angiogenesis drugs, and detection of fluorescence probes in lung tumors.

References

Abdoulaev, G.S. and Hielscher, A.H. (2003), "Three-dimensional optical tomography with the equation of radiative transfer", *J. Electronic Imaging*, Vol. 12 No. 4, pp. 594-601.

Abdoulaev, G.S., Ren, K. and Hielseher, A.H. (2005), "Optical tomography as a PDE-constrained optimization problem", *Inverse Problems*, Vol. 21 No. 5, pp. 1507-30.

Arridge, S.R. and Dorn, O. (2006), "Reconstruction of subdomain boundaries of piecewise constant coefficients of the radiative transfer equation from optical tomography data", *Inverse Problems*, Vol. 22 No. 6, pp. 2175-96.

Aydin, E.D., de Oliveira, C.R.E. and Goddard, A.J.H. (2004), "A finite element-spherical harmonics radiation transport model for photon migration in turbid media", *J. Quant. Spectrosc. Radiat. Transfer*, Vol. 84 No. 3, pp. 247-60.

Aydin, E.D., Katsimichas, S. and de Oliveira, C.R.E. (2005), "Time-dependent diffusion and transport calculations using a finite-element-spherical harmonics method", *J. Quant. Spectrosc. Radiat. Transfer*, Vol. 95 No. 3, pp. 349-63.

Biegler, L., Ghattas, O., Heinkenschloss, M. and van Bloemen Waanders, B. (2003), *Large-scale PDE-constrained Optimization (Lecture Notes in Computational Science and Engineering Vol 30)*, Springer, Berlin.

Bluestone, A.Y., Stewart, M., Lei, B., Kass, I.S., Lasker, J., Abdoulaev, G.S. and Hielscher, A.H. (2004a), "Three-dimensional optical tomographic brain imaging in small animals, Part I: hypercapnia", *Journal of Biomedical Optics*, Vol. 9 No. 5, pp. 1046-62.

Bluestone, A.Y., Stewart, M., Lei, B., Kass, I.S., Lasker, J., Abdoulaev, G.S. and Hielscher, A.H. (2004b), "Three-dimensional optical tomographic brain imaging in small animals, Part I: hypercapnia & Part II: unilateral carotid occlusion", *J. Biomedical Optics*, Vol. 9 No. 5, pp. 1046-173.

Boas, D.A., O'Leary, M.A., Chance, B. and Yodh, A. (1997), "Detection and characterization of optical inhomogeneities with diffuse photon density waves: a signal-to-noise analysis", *Applied Optics*, Vol. 36, pp. 75-92.

Boulanger, J. and Charette, A. (2005a), "Numerical developments for short-pulsed near infra-red laser spectroscopy. Part I: direct treatment", *J Quant. Spectrosc. Radiat. Transfer*, Vol. 91 No. 2, pp. 189-209.

Boulanger, J. and Charette, A. (2005b), "Numerical developments for short-pulsed near infra-red laser spectroscopy. Part II: inverse treatment", *J Quant. Spectrosc. Radiat. Transfer*, Vol. 91 No. 3, pp. 297-318.

Cai, W., Xu, M. and Alfano, R.R. (2003), "Three-dimensional radiative transfer tomography for turbid media", *IEEE J. Sel. Top. Quant.*, Vol. 9 No. 2, pp. 189-98.

Carlson, B.G. and Lathrop, K.D. (1968), "Transport theory – the method of discrete ordinates", in Greenspan, H. (Ed.), *Computing Methods in Reactor Physics*, Gordon and Breach, New York, NY, pp. 166-266.

Cheong, W.F., Prahl, S.A. and Welch, A.J. (1990), "A review of the optical properties of biological tissue", *IEEE J. Quantum Electron*, Vol. 26, pp. 2166-85.

Culver, J.P., Durduran, T., Furuya, D., Cheung, C., Greenberg, J.H. and Yodh, A.G. (2003), "Diffuse optical tomography of cerebral blood flow, oxygenation, and metabolism in rat during focal ischemia", *J. of Cerebral Blood Flow & Metabolism*, Vol. 23, pp. 911-24.

Dorn, O. (1998), "A transport-backtransport method for optical tomography", *Inverse Problems*, Vol. 14, pp. 1107-30.

Duderstadt, J.J. and Martin, W.R. (1979), *Transport Theory*, John Wiley & Sons, New York, NY.

Elliot, R.A., Duracz, T., McCormick, N.J. and Emmons, D.R. (1988), "Experimental test of a time-dependent inverse radiative transfer algorithm for estimating scattering parameters", *J. Opt. Soc. Am. A*, Vol. 5, pp. 366-73.

Frischer, J.S., Huang, J.Z., Serur, A., Kadenhe-Chiweshe, A., McCrudden, K.W., O'Toole, K., Holash, J., Yancopoulos, G.D., Yamashiro, D.J. and Kandel, J.J. (2004), "Effects of potent VEGF blockade on experimental Wilms tumor and its persisting vasculature", *Intl. J. Oncology*, Vol. 25 No. 3, pp. 549-53.

Gibson, A.P., Hebden, J.C. and Arridge, S.R. (2005), "Recent advances in diffuse optical imaging", *Phys. Med. Biol.*, Vol. 50 No. 4, pp. R01-R43.

Glade-Bender, J., Kandel, J.J. and Yamashiro, D.J. (2003), "VEGF blocking therapy in the treatment of cancer", *Expert Opin.Bio. Therapy*, Vol. 3 No. 2, pp. 263-76.

Graves, E.E., Weissleder, R. and Ntziachristos, V. (2004), “Fluorescence molecular imaging of small animal tumor models”, *Current Molecular Medicine*, Vol. 4, pp. 419-30.

Gu, X., Ren, K. and Hielscher, A.H. (2007), “Frequency-domain sensitivity analysis for small imaging domains using the equation of radiative transfer”, *Applied Optics*, Vol. 46 No. 10, pp. 1624-32.

Gulsen, G., Xiong, B., Birgul, O. and Nalcioglu, O. (2006), “Design and implementation of a multifrequency near-infrared diffuse optical tomography system”, *Journal of Biomedical Optics*, Vol. 11 No. 1, 014020.

Hielscher, A.H. (2005), “Optical tomographic imaging of small animals”, *Current Opinion in Biotechnology*, Vol. 16 No. 1, pp. 79-88.

Hielscher, A.H. and Bartel, S. (2001), “Use of penalty terms in gradient-based iterative reconstruction schemes for optical tomography”, *Journal of Biomedical Optics*, Vol. 6 No. 2, pp. 183-92.

Hielscher, A.H., Alcouffe, R.E. and Barbour, R.L. (1998), “Comparison of finite-difference transport and diffusion calculations for photon migration in homogeneous and heterogeneous tissues”, *Phys. Med. Biol.*, Vol. 43, pp. 1285-1302.

Hielscher, A.H., Klose, A.D. and Hanson, K.M. (1999), “Gradient-based iterative image reconstruction scheme for time-resolved optical tomography”, *IEEE Trans. Med. Imag.*, Vol. 18 No. 3, pp. 262-71.

Hielscher, A.H., Klose, A.D., Scheel, A.K., Moa-Anderson, B., Backhaus, M., Netz, U. and Beuthan, J. (2004), “Sagittal laser optical tomography for imaging of rheumatoid finger joints”, *Phys. Med. Biol.*, Vol. 49 No. 7, pp. 1147-63.

Joseph, D.K., Huppert, T.J., Franceschini, M.A. and Boas, D.A. (2006), “Diffuse optical tomography system to image brain activation with improved spatial resolution and validation with functional magnetic resonance imaging”, *Appl. Opt.*, Vol. 45 No. 31, pp. 8142-51.

Joseph, J.H., Wiscombe, W.J. and Weinman, J.A. (1976), “The delta-Eddington approximation for radiative transfer”, *J. Atmos. Sci.*, Vol. 33, pp. 2452--2459.

Khan, T. and Thomas, A. (2005), “Comparison of P-N or spherical harmonics approximation for scattering media with spatially varying and spatially constant refractive indices”, *Opt. Commun.*, Vol. 255 Nos 1/3, pp. 130-66.

Kim, A.D. and Moscoso, M. (2006), “Radiative transport theory for optical molecular imaging”, *Inverse Problems*, Vol. 22 No. 1, pp. 23-42.

Klose, A.D. and Hielscher, A.H. (1999), “Iterative reconstruction scheme for optical tomography based on the equation of radiative transfer”, *Med. Phys.*, Vol. 26 No. 8, pp. 1698-707.

Klose, A.D. and Hielscher, A.H. (2002), “Optical tomography using the time-independent equation of radiative transfer. Part II: inverse model”, *J. Quant. Spectrosc. Radiat. Transf.*, Vol. 72 No. 5, pp. 715-32.

Klose, A.D. and Hielscher, A.H. (2003), “Fluorescence tomography with simulated data based on the equation of radiative transfer”, *Opt. Lett.*, Vol. 28 No. 12, pp. 1019-21.

Klose, A.D. and Larsen, E.W. (2006), “Light transport in biological tissue based on the simplified spherical harmonics equations”, *Journal of Computational Physics*, Vol. 220, pp. 441-70.

Klose, A.D., Ntziachristos, V. and Hielscher, A.H. (2004), “*In vivo* fluorescence molecular imaging with a radiative transfer model”, *Molecular Imaging*, Vol. 3 No. 3, p. 230.

Klose, A.K., Ntzachristos, V. and Hielscher, A.H. (2005), “The inverse source problem based on the radiative transfer equation in molecular optical imaging”, *J. Computational Physics*, Vol. 202, pp. 323-45.

Larsen, E.W. (1981), "Solution of the inverse problem in multigroup transport theory", *J. Math. Phys.*, Vol. 22, pp. 158-60.

Lasker, J.M., Masciotti, J., Schoenecker, M., Schmitz, C. and Hielscher, A. (2007), "Digital detection techniques for dynamic optical tomographic imaging", in Chance, B., Alfano, R.R., Tromberg, B.J., Tamura, M. and Sevick-Muraca, E.M. (Eds), *Proceedings of SPIE – Volume 6434 Optical Tomography and Spectroscopy of Tissue VII*, 64341T.

Li, C., Zhao, H., Anderson, B. and Jiang, H. (2006), "Multispectral breast imaging using a ten-wavelength, 64 × 64 source/detector channels silicon photodiode-based diffuse optical tomography system", *Medical Physics*, Vol. 33 No. 3, pp. 627-36.

McBride, T.O., Pogue, B.W., Jiang, S., Osterberg, U.L. and Paulsen, K.D. (2001), "A parallel-detection frequency-domain near-infrared tomography system for hemoglobin imaging of the breast *in vivo*", *Review of Scientific Instruments*, Vol. 72 No. 3, pp. 1817-24.

McCormick, N.J. (1992), "Inverse radiative transfer problems: a review", *Nucl. Sci. Eng.*, Vol. 112, pp. 185-98.

Masciotti, J., Abdoulaev, G., Provenzano, F., Hur, J., Papa, J., Bae, J., Huang, J., Yamashiro, D., Kandel, J. and Hielscher, A.H. (2005), "Optical tomographic and magnetic resonance imaging of tumor growth and regression in mice with VEGF blockade", paper presented at 27th Annual International Conference of the IEEE Engineering in Medicine and Biology Society (Institute of Electrical and Electronics Engineers, Shanghai, 2005).

Patwardhan, S., Bloch, S., Achilefu, S. and Culver, J. (2005), "Time-dependent whole-body fluorescence tomography of probe bio-distributions in mice", *Optics Express*, Vol. 13 No. 7, pp. 2564-77.

Pomper, M.G. (2002), "Can small animal imaging accelerate drug development?", *J. Cell. Biochem. Suppl.*, Vol. 39, pp. 211-20.

Ren, K., Bal, G. and Hielscher, A.H. (2006), "Frequency domain optical tomography based on the equation of radiative transfer", *SIAM J. Sci. Comput.*, Vol. 28 No. 4, pp. 1463-89.

Ren, K., Abdoulaev, G.S., Bal, G. and Hielscher, A.H. (2004), "Algorithm for solving the equation of radiative transfer in the frequency domain", *Opt. Lett.*, Vol. 29 No. 6, pp. 578-80.

Scheel, A.K., Backhaus, M., Klose, A.D., Moa-Anderson, B., Netz, U., Hermann, K.G., Beuthan, J., Muller, G.A., Burmester, G.R. and Hielscher, A.H. (2005), "Comparison of sagittal laser optical tomography with ultrasound and clinical examination for diagnosis of synovitis in PIP joints", *Annals of the Rheumatic Diseases*, Vol. 64, pp. 239-45.

Schmidt, F.E.W., Fry, M.E., Hillman, E.M.C., Hebden, J.C. and Delpy, D.T. (2000), "A 32-channel time-resolved instrument for medical optical tomography", *Review of Scientific Instruments*, Vol. 71 No. 1, pp. 256-65.

Schmitz, C.H., Löcker, M., Lasker, J.M., Hielscher, A.H. and Barbour, R.L. (2002), "Instrumentation for fast functional optical tomography", *Review of Scientific Instrumentation*, Vol. 73 No. 2, pp. 429-39.

Siegel, A.M., Culver, J.P., Madeville, J.B. and Boas, D.A. (2003), "Temporal comparison of functional brain imaging with diffuse optical tomography and fMRI during rat forepaw stimulation", *Physics in Medicine and Biology*, Vol. 48, pp. 1391-403.

Tarvainen, T., Vauhkonen, M. and Kolehmainen, V. (2005a), "Coupled radiative transfer equation and diffusion approximation model for photon migration in turbid medium with low-scattering and non-scattering regions", *Phys. Med. Biol.*, Vol. 50 No. 20, pp. 4913-30.

Tarvainen, T., Vauhkonen, M. and Kolehmainen, V. (2005b), "Hybrid radiative-transfer-diffusion model for optical tomography", *Appl. Optics*, Vol. 44 No. 6, pp. 876-86.

Tarvainen, T., Vauhkonen, M. and Kolehmainen, V. (2006), "Finite element model for the coupled radiative transfer equation and diffusion approximation", *Int. J. Numer. Meth. Eng.*, Vol. 65 No. 3, pp. 383-405.

Thompson, A.B. and Sevick-Muraca, E.M. (2003), "Near-infrared fluorescence contrast-enhanced imaging with intensified charge-coupled device homodyne detection: measurement precision and accuracy", *Journal of Biomedical Optics*, Vol. 8, pp. 111-20.

Toronov, V., D'Amico, E., Hueber, D., Gratton, E., Barbieri, B. and Webb, A. (2003), "Optimization of the signal-to-noise ratio of frequency-domain instrument for near-infrared spectro-imaging of the human brain", *Optics Express*, Vol. 11, pp. 2117-729.

Wang, A.P. and Ueno, S. (1989), "An inverse problem in a three-dimensional radiative transfer", *Astrophys. Space Sci.*, Vol. 155, pp. 105-11.

Weissleder, R. and Mahmood, U. (2001), "Molecular imaging", *Radiology*, Vol. 219, p. 316.

Corresponding author
Alexander D. Klose can be contacted at: ak2083@columbia.edu